

Multiscale spatial analysis of fracture nodes in two dimensions

Mahmood Shakiba ^{a,*¹}, Larry W. Lake ^a, Julia F.W. Gale ^b, Stephen E. Laubach ^b, Michael J. Pyrcz ^{a,b,c}

^a Hildebrand Department of Petroleum and Geosystems Engineering, The University of Texas at Austin, USA

^b Bureau of Economic Geology, Jackson School of Geosciences, The University of Texas at Austin, USA

^c Department of Geological Sciences, Jackson School of Geosciences, The University of Texas at Austin, USA



ARTICLE INFO

Keywords:
Fracture arrangement
Spatial pattern
Ripley's *K*-Function
Point processes

ABSTRACT

Spatial arrangement of fractures as a function of scale is an important component of fracture quantification for inferential and predictive modeling. Available methods that analyze fracture spatial arrangement are based on one-dimensional spacing data; therefore, they are limited to semi-parallel fractures. Such methods cannot be applied to fracture networks in higher dimensions, particularly when fractures have different orientations. To characterize fracture arrangements in two dimensions, we propose using Ripley's *K*-function, as a method of point pattern analysis, to quantify spatial arrangement of fracture nodes. Fracture nodes, such as barycenters, intersection points, and tips, are point-based representations of fracture locations and connectivity within the fracture network. We introduce formulations for isotropic as well as directional analyses of spatial arrangement. In addition, we derive formulations for edge correction in circular and rectangular study domains. Finally, we demonstrate applications of Ripley's *K*-function on two natural fracture datasets. Our proposed method supports quantification and characterization of fracture spatial arrangements that allow practitioners to build representative models of fractures in the subsurface.

Plain language summary

Fracture locations and proximity in the subsurface may significantly affect rock properties and flow characteristics. Spatial distribution of fractures can be analyzed using a metric called spatial arrangement, which describes how fractures are positioned with respect to each other at different length scales. Fracture spatial arrangements are traditionally quantified using one-dimensional measurements of spacings between semi-parallel fractures. In this work, we propose a new method for calculating spatial arrangement of fractures in two dimensions using point populations that are extracted from fracture traces. These point populations are fracture barycenters, intersections, and tips. To quantify two-dimensional spatial arrangements, we use a method of point pattern analysis called Ripley's *K*-function. Using the *K*-function, we identify point spatial arrangements that are clustered or antoclustered. Our proposed method helps researchers and practitioners to better characterize fracture networks and to build representative models of subsurface rock formations.

1. Introduction

Spatial analysis of fractures is a topic of interest in many subsurface applications because fracture locations, proximity, and interactions within a network may significantly control rock properties, geomechanical characteristics, and flow through porous media (e.g., Narr et al., 2006; Olson, 2008; Weng et al., 2011; Hardebol et al., 2015; Laubach et al., 2019). One of the most informative metrics used in fracture spatial analysis is fracture arrangement (e.g., Odling, 1997; Laubach et al., 2018; Marrett et al., 2018; Sanderson and Peacock, 2019; Bistacchi et al., 2020). Spatial arrangement is an attribute that describes how arrays of objects are placed in a space. The locations and distances between objects determine the type of spatial arrangements.

Two fracture networks with similar orientations and length distributions may exhibit different spatial arrangements if fractures are positioned following different patterns, as illustrated in Fig. 1. In this figure, both networks have identical distributions of fracture length and orientation, but they exhibit different spatial arrangements and fracture

* Corresponding author.

E-mail address: m_shakiba@utexas.edu (M. Shakiba).

¹ Present Address: The University of Texas at Austin Hildebrand Department of Petroleum and Geosystems Engineering 200 E. Dean Keeton St., Stop C0300 Austin, TX 78712-1585.

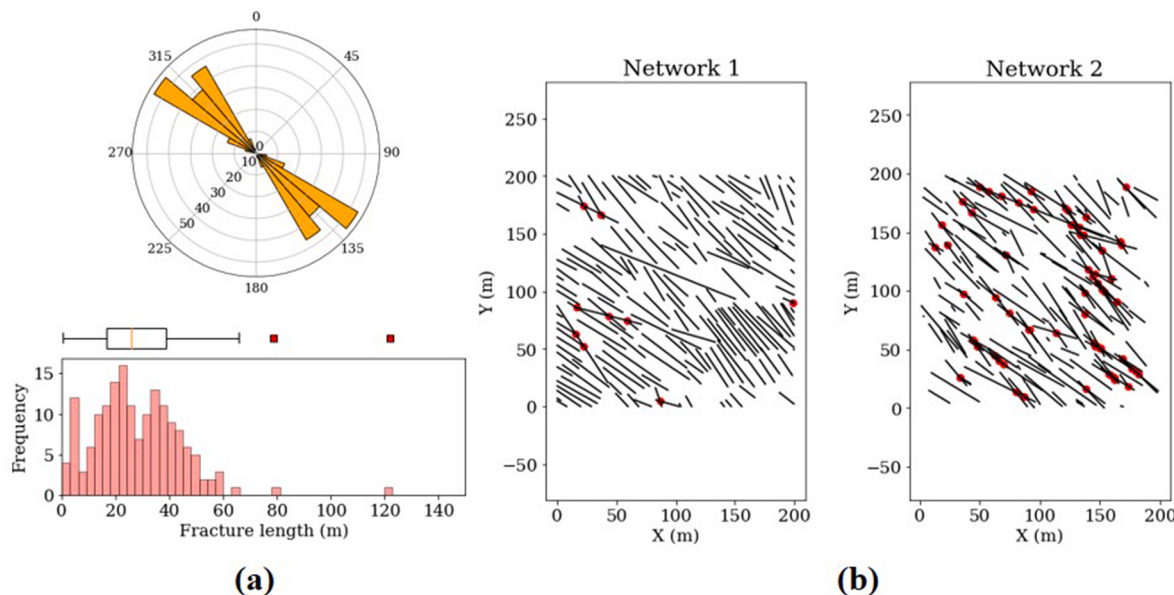


Fig. 1. Comparison of spatial arrangements in two synthetic fracture networks. (a) Both fracture networks have identical distributions of fracture length and strike angle. (b) However, they exhibit different degrees of connectivity. In network 1, connectivity is limited, whereas in network 2, fractures are connected throughout the study domain. Fracture intersections are shown as red dots.

intersection patterns. The fracture intersection in network 1 is very limited, whereas in network 2, fractures are connected over a large area inside the study domain. As fracture connectivity is one of the important factors that control flow behavior of subsurface formations, fluid flow and transport properties might be different in these two fracture networks.

Several methods are available that describe spatial arrangement of fractures, such as Fourier and wavelet analysis (e.g., Hare, 2002; Rizzo et al., 2018); lacunarity (e.g., Roy et al., 2014); and correlation count (e.g., Laubach et al., 2018; Marrett et al., 2018; Wang et al., 2019). However, these methods are primarily formulated for one-dimensional fracture measurements, such as from outcrop scanlines, borehole image logs, and cores. These one-dimensional methods use spacings between fractures that are measured along a sampling line interval and therefore are limited to populations of semi-parallel fractures.

Many recent outcrop fracture measurements are performed in two dimensions via aerial imaging using satellites, airplanes, and drones (e.g., Bemis et al., 2014; Vollgiger and Cruden, 2016). Two-dimensional fracture measurements are more informative than one-dimensional measurements because they record trace lengths, strike angles, density, intensity, and topological elements in addition to spacing between fractures. Therefore, development of methods that analyze spatial arrangement of fractures in two dimensions is valuable for understanding geometrical pattern of fractures.

Some of the common spatial analysis techniques for fractures in two dimensions are box counting (e.g., Barton and Larsen, 1985; Gillespie et al., 1993; Walsh and Watterson, 1993; Bonnet et al., 2001), mass method (e.g., Sornette and Davy, 1991; Bonnet et al., 2001), and circular scanlines (e.g., Mauldon et al., 2001; Rohrbaugh et al., 2002). These methods follow a window-sampling scheme, and they quantify spatial distribution of fractures based on fracture counts or trace lengths corresponding to different window sizes. These methods can be further improved by integrating the sequence and distances between fractures to reveal additional information on spatial arrangement of fractures in two dimensions.

In two dimensions, measuring distances between semi-planar fractures with various lengths and orientations is not straightforward. One method may use the shortest distance between fracture traces as the distance between fractures, whereas another may take the distance

between fracture tips as the distance between fractures. To make the measurement of distances in two dimensions unambiguous, one solution is to use nodes and point sets that can be extracted from fracture traces such as fracture intersection points, abutments, tips, and barycenters (midpoints).

Commonly, the counts and proportion of fracture nodes are used to investigate fracture topology, network percolation, and spatial correlation (e.g., Manzocchi, 2002; Sævik and Nixon, 2017; Hanke et al., 2018; Sanderson and Nixon, 2018; Forstner and Laubach, 2022). In addition, visual inspection of the density or intensity maps of fracture nodes may provide a preliminary view of clustering or randomness of fractures. However, statistical significance of a fracture clustering or randomness cannot be evaluated by a visual inspection. To identify the threshold above or below which fracture nodes transition from one arrangement to another, a quantitative statistical analysis is needed.

Transformation of fracture networks into nodes and point sets allows practitioners to use a new class of methods to study spatial arrangement of fractures in two dimensions. One of the conventional methods in spatial analysis of point patterns is Ripley's K-function (Ripley, 1976, 1977; Baddeley et al., 2007; Dixon, 2014; Cressie, 2015). Shakiba et al. (2022, 2023a) introduced one-dimensional formulations of Ripley's K-function for fracture spatial analysis, and they demonstrated various characterization and modeling applications. Although Ripley's K-function has shown promising applications in many fields, it has received little or no attention in rock fracture spatial analysis. This could be because Ripley's K-function is primarily formulated for spatial analysis of discrete points with well-defined pairwise-distances, whereas fractures are two- or three-dimensional surfaces with trace length and orientation.

We propose a new workflow that deploys Ripley's K-function to study two-dimensional spatial arrangement of fractures by transforming fracture networks into various nodes such as fracture intersection points, abutments, tips, and barycenters. Fracture nodes are point-based representation of fracture locations and connectivity throughout the fracture network. We also develop edge correction for Ripley's K-function in rectangular and circular study domains. To identify the statistical significance of fracture arrangements, we calculate the confidence interval for random arrangements using Monte Carlo simulations.

In the next sections, we introduce isotropic as well as directional

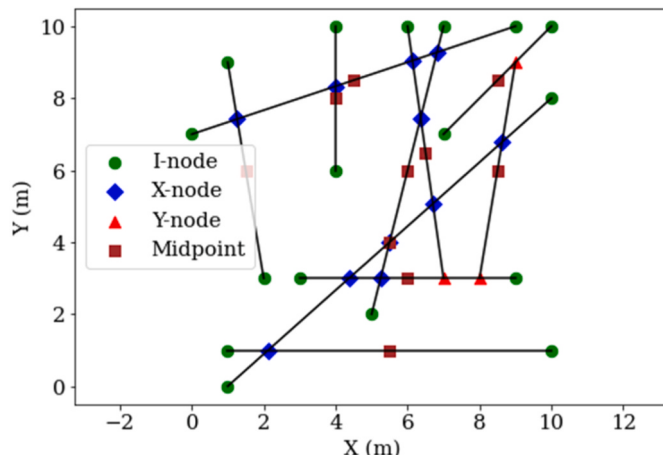


Fig. 2. Schematic illustration of I-nodes (terminations), X-nodes (intersections), Y-nodes (abutments), and midpoints in a fracture network.

formulations of Ripley's K -function and use two natural fracture datasets to demonstrate applications of the K -function in two dimensions.

2. Methodology

The two-dimensional formulations of Ripley's K -function apply to point populations using the distances between points to describe spatial arrangements. Therefore, the first step is to extract various populations of points (nodes) from fracture traces.

2.1. Transforming fracture networks into point patterns

One approach is to extract barycenters. In two dimensions, barycenters are the midpoints of fracture traces. Fracture midpoints are surrogates for fracture locations. Spatial analysis of midpoints provides insights into the degree of proximity between fractures inside the study area. Another approach is to extract fracture nodes that describe network topology: I-nodes, X-nodes, and Y-nodes. I-nodes are isolated tips where fractures terminate. X-nodes are the crossings between fractures, and Y-nodes are where one fracture abuts against or splays from another fracture (e.g., Manzocchi, 2002; Sanderson and Nixon, 2015). Spatial arrangements of X-nodes and Y-nodes (fracture connections) represent the degree of connection between fractures across the study area. On the other hand, fracture I-nodes could be another surrogate for fracture locations similar to midpoints while integrating fracture extent, because I-nodes mark the endpoints of fracture traces. An example of fracture nodes and midpoints is shown in Fig. 2.

2.2. Ripley's K -function

Ripley's K -function (hereinafter K -function) applies to an array of points, and it takes scale as a primary variable in spatial analysis. This makes the K -function well suited for studying multiscale characteristics of fracture arrangements. The two-dimensional formulations of the K -function can be derived for omnidirectional and directional analyses.

2.2.1. Omnidirectional K -function

In two dimensions, the omnidirectional formulation of the K -function is calculated using the expected number of points (nodes) that fall within a circular search window of radius h placed on a random point inside the study domain, and it is normalized by the overall point intensity λ . The point intensity λ is the total number of points N divided by the area of the study domain A (i.e., $\lambda = N/A$). Calculation of the omnidirectional K -function involves placing a circle of radius h on every point inside the study domain and counting the number of neighboring points that fall inside the circle (Fig. 3). The weighted average number of neighbors is then divided by the point intensity to calculate the omnidirectional K -function at the length scale h . Therefore,

$$K^{2D}(h) = \frac{\text{Expected } \# \text{ of neighbors}}{\lambda} = \frac{A}{N^2} \sum_{i=1}^N \sum_{j=1 \mid j \neq i}^N \omega_i \times H[h - d(i,j)] \quad (1)$$

where $d(i,j) = \sqrt{(x_i - x_j)^2 + (y_i - y_j)^2}$ is the distance between points i and j ; H is the Heaviside step function (which returns 0 for $h - d(i,j) < 0$, and 1 otherwise); and ω_i is a weighting factor to correct for edge effects. In the following sections, we drop the 2D superscript in the K -function notation for brevity.

The K -functions are calculated over a range of length scales by changing the diameter of the search window. The largest length scale in that range is usually the diameter of the study domain, and the smallest length scale is the minimum distance between any two points inside the domain. Because fracture length scales often span multiple orders of magnitude, a logarithmic series of length scales can be sampled from the range of analysis.

In a fully random point pattern, the expected number of neighboring points that fall inside a circular search window of radius h equals the point intensity times the area of the window ($\lambda \times \pi h^2$). Therefore, the omnidirectional K -function for a randomly distributed point pattern is

$$K_{\text{random}}(h) = \frac{\text{Expected } \# \text{ of neighbors}}{\lambda} = \frac{\lambda \times \pi h^2}{\lambda} = \pi h^2 \quad (2)$$

which is the area of the search window. To identify clustered and anti-clustered arrangements in a point pattern, the calculated K -functions are benchmarked against $K_{\text{random}}(h)$ at the same scales. To facilitate comparison, we can normalize the K -function by $K_{\text{random}}(h)$. Thus,

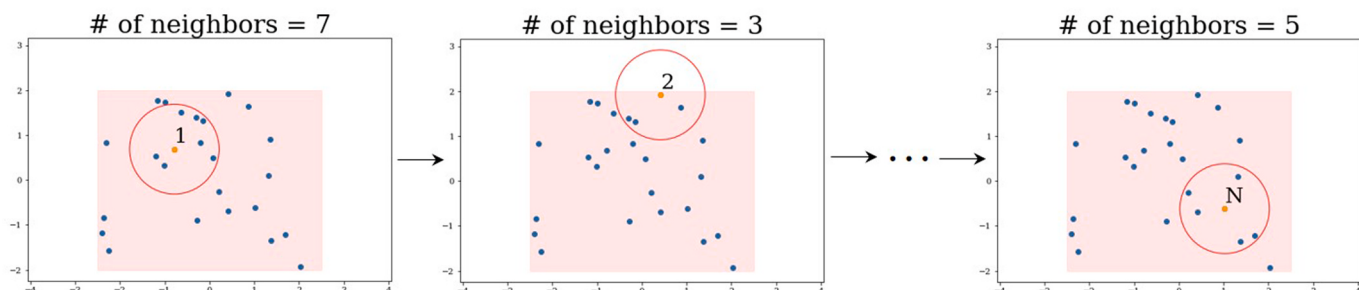


Fig. 3. Schematic example of the two-dimensional point-counting procedure used in omnidirectional K -function calculation. A circle of radius h is placed on every point inside the study domain to count the number of neighboring points. Weighted average number of neighbors is then divided by point intensity to calculate the omnidirectional K -function at length scale h .

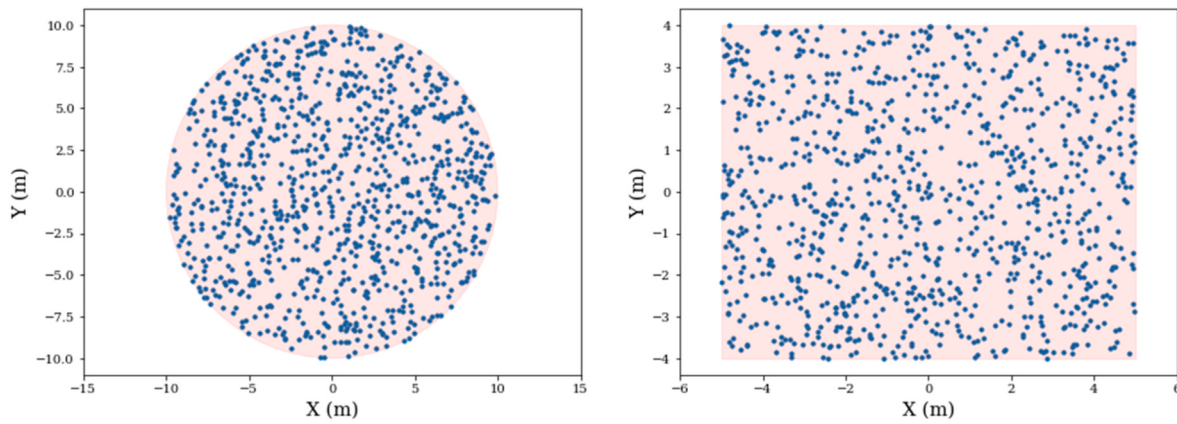


Fig. 4. Sample realizations of random arrangements in circular and rectangular study domains. Each realization has 1000 data points.

$$K_n(h) = \frac{K(h)}{K_{\text{random}}(h)} = \frac{A}{\pi h^2 N^2} \sum_{i=1}^N \sum_{j=1, j \neq i}^N \omega_i \times H[h - d(i,j)] \quad (3)$$

Therefore, for a random point pattern the expected normalized K -function is

$$K_{n, \text{random}}(h) = \frac{\pi h^2}{\pi h^2} = 1 \quad (4)$$

The $K_n(h)$ values greater than 1 indicate point clustering, whereas lower values indicate antclustering. To identify clustered or antoclustered arrangements that are statistically significant, the confidence interval for random arrangements is calculated using spatial random realizations generated by Monte Carlo simulation. The boundaries of the confidence interval at each length scale are the K -functions above or below which point patterns transition from one arrangement to another. Therefore, a confidence interval provides a metric for identifying spatial arrangements that are statistically significant, an inference that cannot be reached merely by visual inspection of point patterns.

2.2.2. Edge correction

For the data points that are near the edge or boundary, part of the circular search window may fall outside the study domain (for instance, point 2 in Fig. 2). This results in an effectively smaller search area and consequently fewer neighbors counted around the boundary points. Because of this bias in the point-counting procedure, values of the K -function are underestimated. To correct for edge effects, a weighting

factor is proposed by Ripley (1976, 1977) to inflate the number of neighbors in the K -function formulations (ω_i in Eqs. (1), (3), (6), and (8)). In two dimensions, this weighting factor is inversely proportional to the fraction of the search window that overlaps with the study domain.

$$\omega_i = \frac{\pi h^2}{A_{\text{inside}}} \quad (5)$$

For points that are fully inside the study domain, such as point 1 in Fig. 2, the weighting factor is 1, and for boundary points the weighting factor is greater than 1.

Depending on the shape of the study domain and the position of the circular search window, the magnitude of A_{inside} and the corresponding weighting factor will be different. Closed-form derivations of the weighting factors for edge correction in circular and rectangular study domains are given in the Appendix.

2.2.3. Omnidirectional K -function for random point patterns

To verify the implementation of the K -function and edge correction in two dimensions, the omnidirectional K -function is calculated for random point patterns in circular and rectangular study domains. The expected values (50th percentile) of the K -function at each length scale for 100 realizations of random point patterns are compared against the analytical expressions given in Eqs. (2) and (4). Each realization has 1000 points placed randomly inside the study domain. The radius of the circular study domain is 10 m, and the dimensions of the rectangular study domain are 10 m and 8 m. Two sample realizations are shown in

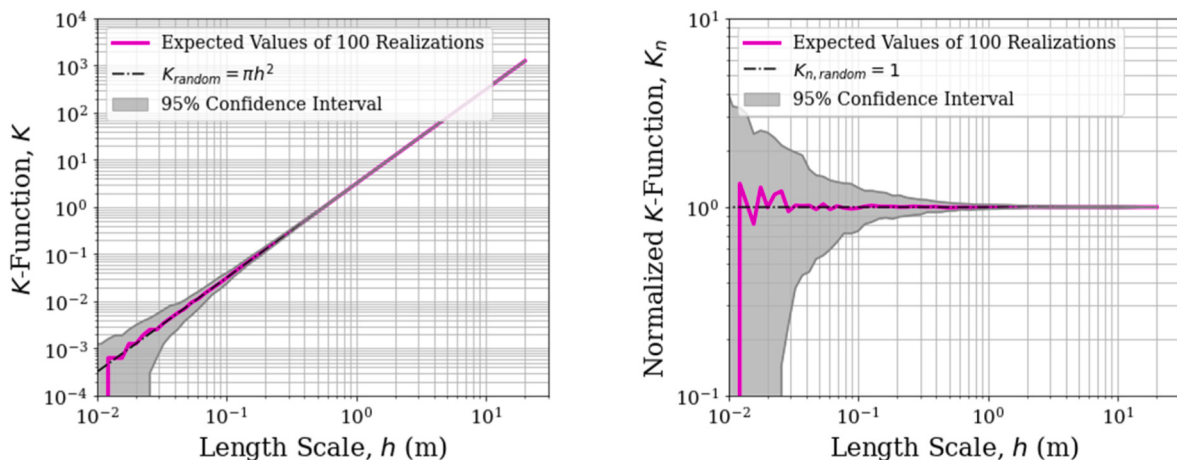


Fig. 5. Spatial analysis of random arrangements in a circular study domain of radius 8 m. Expected values of the omnidirectional $K(h)$ (left) and normalized omnidirectional $K_n(h)$ (right) are calculated for 100 realizations. Each realization has 1000 data points. The 95% confidence intervals are shaded in gray.

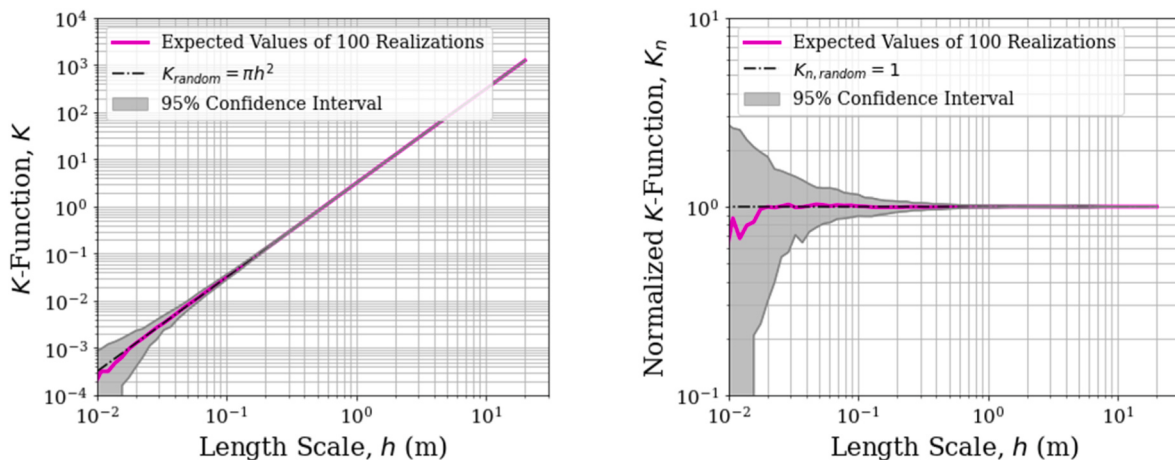


Fig. 6. Spatial analysis of random arrangements in a rectangular study domain of size $10\text{ m} \times 8\text{ m}$. Expected values of the omnidirectional K -function $K(h)$ (left) and normalized omnidirectional K -function $K_n(h)$ (right) are calculated for 100 realizations. Each realization has 1000 data points. The 95% confidence intervals are shaded in gray.

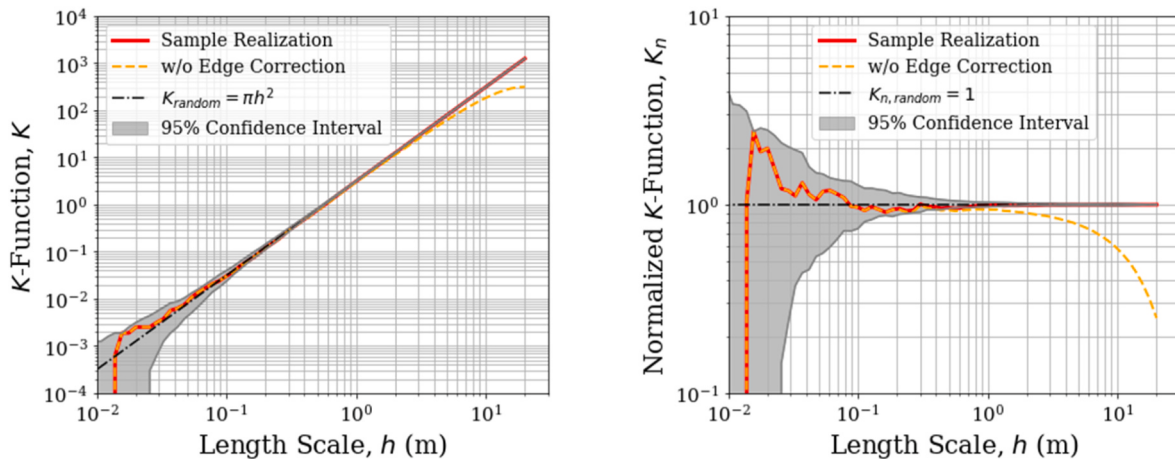


Fig. 7. Impact of edge effect on K -function analysis. The omnidirectional K -function (left) and normalized omnidirectional K -function (right) are calculated for the sample realization in the circular study domain in Fig. 4 with and without edge correction. Without edge correction, the omnidirectional K -function and normalized omnidirectional K -function are underestimated.

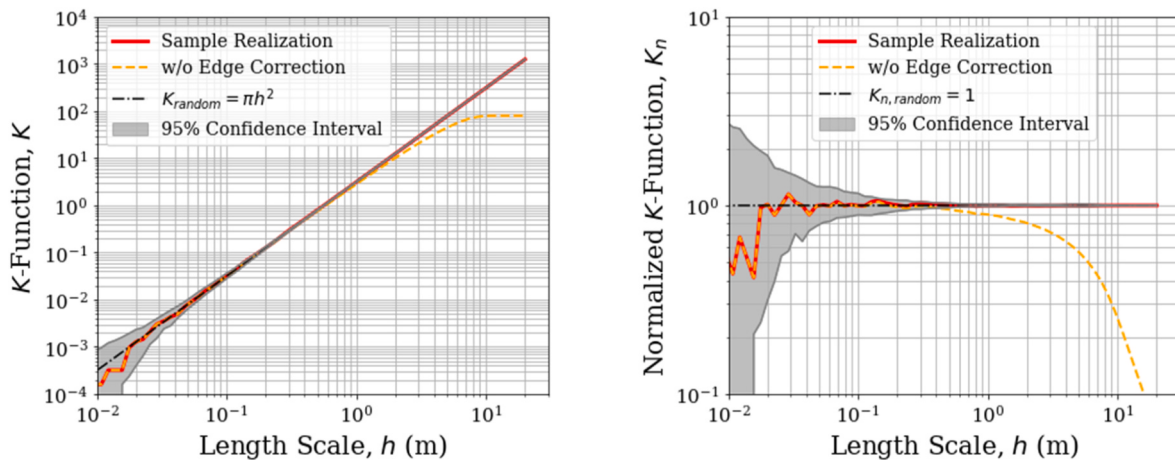


Fig. 8. Impact of edge effect on the K -function analysis. The omnidirectional K -function (left) and normalized omnidirectional K -function (right) are calculated for the sample realization in the rectangular study domain in Fig. 4 with and without edge correction. Without edge correction, the omnidirectional K -function and normalized omnidirectional K -function are underestimated.

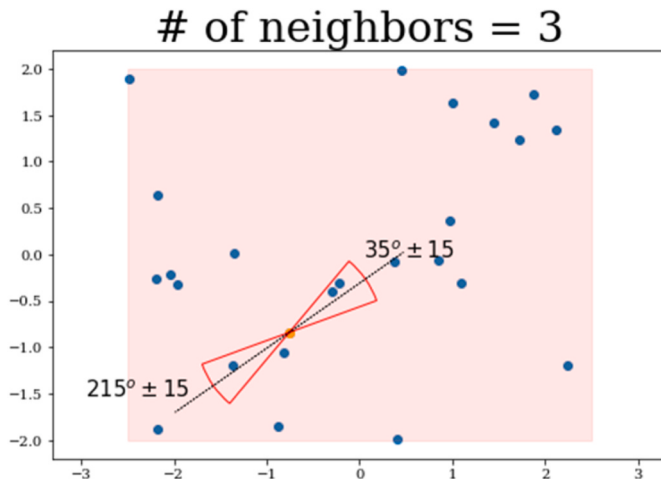


Fig. 9. Example of a directional search window used in point-counting procedure. Search window is along the 35-degree azimuth ($\theta = 35^\circ$), and azimuth tolerance is 15° ($\Delta\theta = 15^\circ$).

Fig. 4.

The confidence intervals and the expected values of the omnidirectional K -function and the normalized omnidirectional K -function calculated from 100 random point patterns are illustrated in Figs. 5 and 6 for the circular and rectangular study domains, respectively. Expected values of K and K_n agree well with the analytical formulations. Fluctuations at small length scales are because of the insufficient number of points sampled at those scales. Increasing the number of data points inside the study domain would dampen these fluctuations, and the expected values converge to the analytical solution at small length scales. These results confirm the accuracy of the K -function implementation.

In addition, to highlight the impact of edge effects, the omnidirectional K -functions for the sample realizations in Fig. 4 are calculated with and without edge correction (Figs. 7 and 8). As previously mentioned, results indicate that the K -functions without edge correction underestimate the true values. Without edge correction, the deviation from the true K -function becomes more significant at larger length scales because it would be more likely that part of the search window falls outside the boundaries of the study domain.

2.2.4. Directional K -function

In the omnidirectional K -function, a circular search window is placed on every point to count the number of neighbors (Fig. 2). Using a full

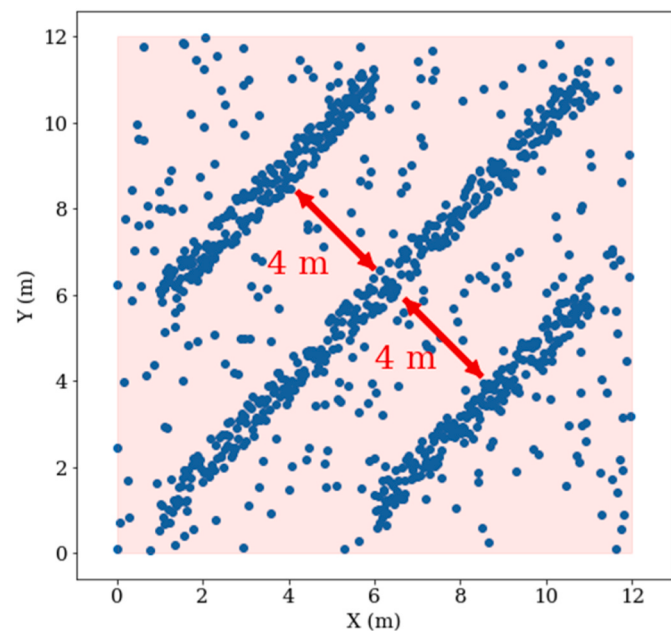


Fig. 10. A synthetic point pattern with three parallel linear-shaped clusters oriented along the 45-degree azimuth. Distances between clusters are approximately 4 m.

also as a function of azimuth. Therefore, the circular search window is replaced by two symmetric sectors along the azimuth of interest θ . The angle of sectors is twice the azimuth tolerance, $2\Delta\theta$. An example of a directional (azimuthal) search window is shown in Fig. 9. The azimuth angles are measured clockwise from the top.

Therefore, the directional K -function (also called azimuthal K -function) is derived by adding a term to Eq. (1) to filter out neighboring points based on their directions in addition to their separation distances.

$$K^\theta(h) = \frac{A}{N^2} \sum_{i=1}^N \sum_{j=1, j \neq i}^N \omega_i \times H[h - d(i, j)] \times F[\theta, \theta_{ij}, \Delta\theta] \quad (6)$$

where F is a function that returns 1 if the angle of the line connecting points i and j , θ_{ij} , is within the azimuth tolerance (i.e., $\theta - \Delta\theta \leq \theta_{ij} < \theta + \Delta\theta$), and returns 0 otherwise. For a fully random pattern, the expected value of the directional K -function with search sectors of radius h and azimuth tolerance of $\Delta\theta$ is calculated as follows.

$$K_{random}^\theta(h) = \frac{\text{Expected } \# \text{ of neighbors}}{\lambda} = \frac{\text{intensity} \times \text{area of two sectors of angle } 2\Delta\theta}{\lambda} = \frac{\lambda \times 2 \times \pi h^2 \times \frac{2\Delta\theta}{360}}{\lambda} = \frac{\pi h^2 \Delta\theta}{90} \quad (7)$$

circle implicitly assumes that the underlying point pattern is isotropic. In an isotropic point pattern, direction is not important, and spatial arrangements will be similar regardless of the azimuth along which points are analyzed. However, fractures in the subsurface may propagate and intersect in specific directions because of different magnitudes of principal stresses, heterogeneous rock properties, formation bedding, and other factors. Therefore, an omnidirectional K -function fails to account for directionalities in fracture networks.

To make the K -function suitable for anisotropic point patterns, the search window in the point-counting procedure should be modified such that it filters neighboring points not only as a function of distance but

We normalize the directional K -function with the expected value of a random arrangement.

$$K_n^\theta(h) = \frac{90A}{\pi h^2 \Delta\theta N^2} \sum_{i=1}^N \sum_{j=1, j \neq i}^N \omega_i \times H[h - d(i, j)] \times F[\theta, \theta_{ij}, \Delta\theta] \quad (8)$$

Similar to the omnidirectional K -function, the $K_n^\theta(h)$ values greater than 1 indicate point clustering along the azimuth of θ , whereas lower values indicate antclustering. The statistically significant clustered or antoclustered arrangements are identified by comparing them against the confidence interval for $K_{random}^\theta(h)$ of random arrangements.

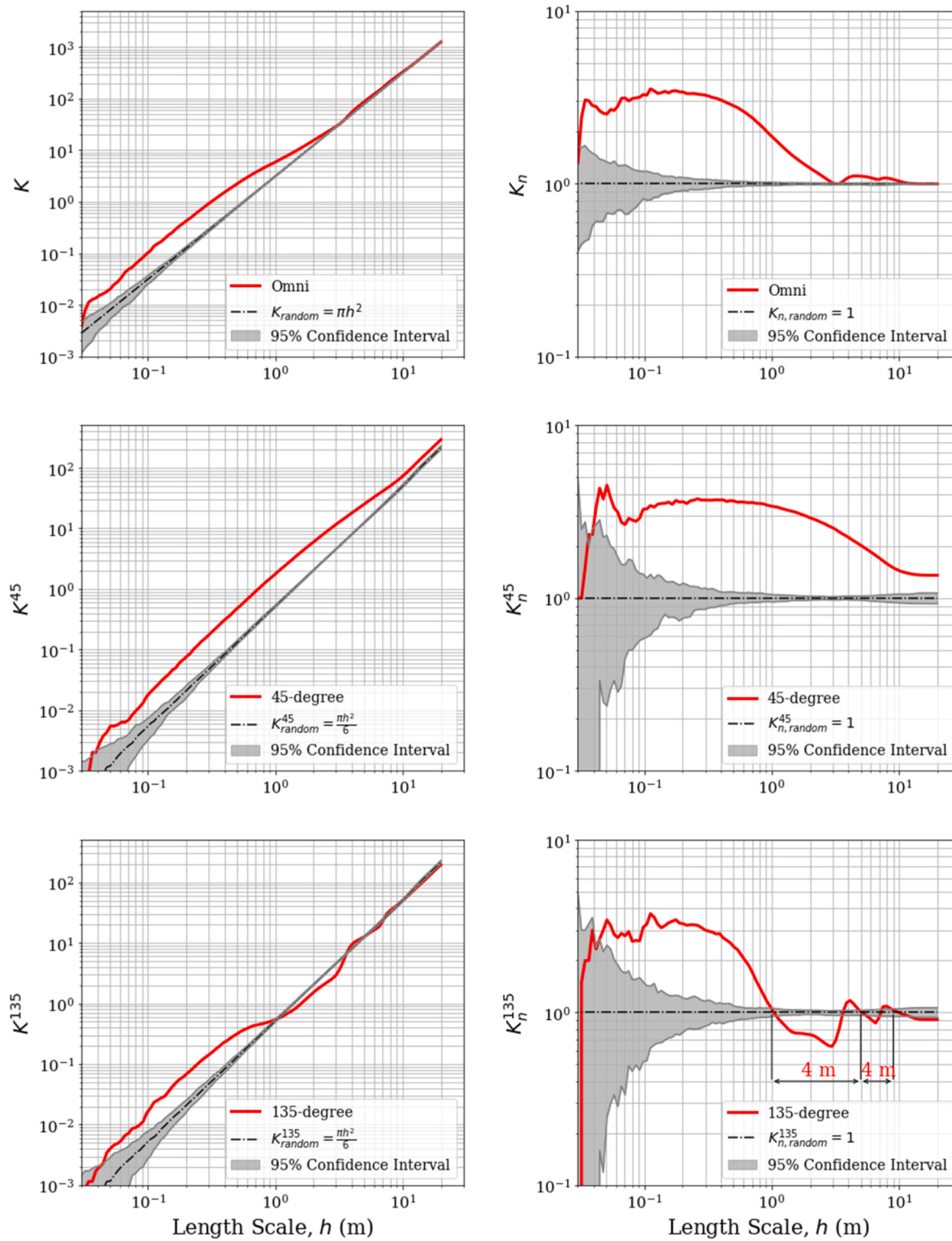


Fig. 11. Omnidirectional and directional K -functions and normalized K -functions calculated using the synthetic example in Fig. 10. Directional K -functions are calculated along 45-degree and 135-degree azimuths.

The following synthetic example highlights our application of the directional K -function. In this example, 1000 points are distributed inside a $12\text{ m} \times 12\text{ m}$ square domain (Fig. 10). The points form three parallel linear-shaped clusters that are approximately 4 m apart. The clusters are all oriented in the diagonal direction, parallel to the 45-degree azimuth, and they form a cyclicity in the perpendicular direction, parallel to the 135-degree azimuth. To analyze the spatial arrangement

of points, the directional K -functions are calculated for the 45- and 135-degree azimuths with 15° tolerance, and results are compared against the omnidirectional K -functions.

Fig. 11 indicates the omnidirectional and directional K -functions calculated for the point pattern in Fig. 10. The omnidirectional K -function is above the confidence interval at length scales smaller than 3.6 m and between 3.6 and 14.4 m. Although the omnidirectional K -

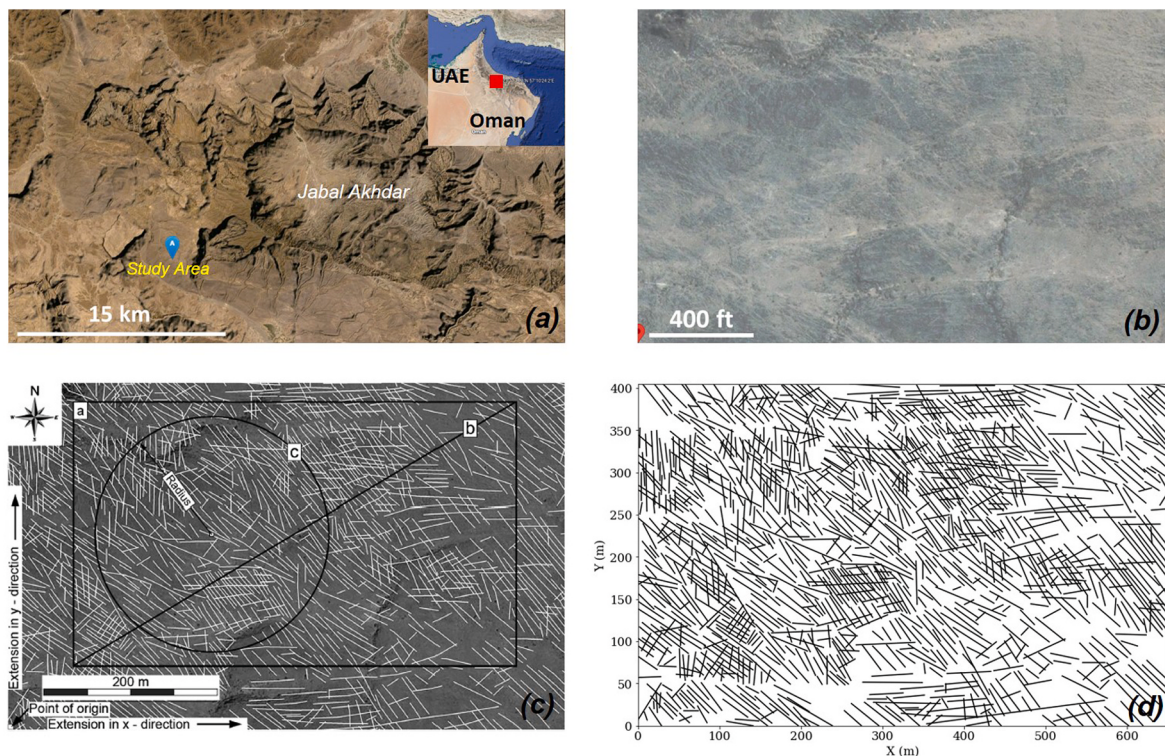


Fig. 12. Fracture network at Jabal Akhdar, Oman. (a) Satellite image of Jabal Akhdar dome and study area on the southern flank (from Geoplaner v3.1). (b) Aerial view of study area (from Google Maps). (c) Manually identified lineaments (from Zeeb et al., 2013). (d) Digitized fracture network. The latitude and longitude of the lower left corner are 23°11'14.1"N and 57°10'24.2"E, respectively.

function correctly identifies the clustered arrangement, it provides no information on the anisotropic trends in the point pattern. In addition, at large length scales, for instance larger than 14.4 m, the omnidirectional K -function falls inside the confidence interval and the spatial arrangement becomes indistinguishable from random, because the impact of clustering along the 45-degree azimuth is averaged and canceled by the intermediate anticlustered points. On the other hand, the directional K -function along the 45-degree azimuth shows a persistent clustered arrangement across all length scales larger than 4×10^{-2} m. In other words, regardless of the size of length scale, the expected number of neighboring points is statistically greater than that of a random pattern if traversing along the 45-degree azimuth parallel to the orientation of the clusters. Moreover, the K -function along the 135-degree azimuth shows sinusoidal characteristics, in which the K -function oscillates around the expected values of random arrangements. This characteristic is similar to the semivariograms of cyclic patterns, also known as the “hole effect” (e.g., Pyrcz and Deutsch, 2003). Along the 135-degree azimuth, the search window samples from clustered structures and

intermediate anticlustered points. Therefore, the spatial arrangement alternates between being clustered and anticlustered. The cycles repeat approximately every 4 m, which is consistent with the distances between the clusters observed in the point pattern.

This example clearly indicates that the directional K -functions are more informative than the omnidirectional counterparts. The directional K -function can accurately identify major anisotropic directions and also estimate the distances between clustered structures in datasets. Our approach can usefully be combined with other methods to capture the extended nature of fractures (e.g., Corrêa et al., 2022). In the next section, we use the K -function in two dimensions to study natural fracture datasets.

3. Results

The omnidirectional and directional K -functions introduced above are used in this section to study the spatial arrangements of fracture nodes, midpoints, endpoints, and intersection points in two natural

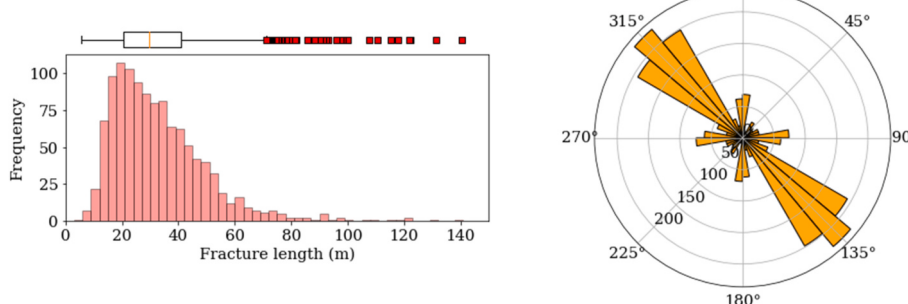


Fig. 13. Histogram and box plot of fracture length (left) and rose diagram of fracture strike angle (right) at Jabal Akhdar, Oman.

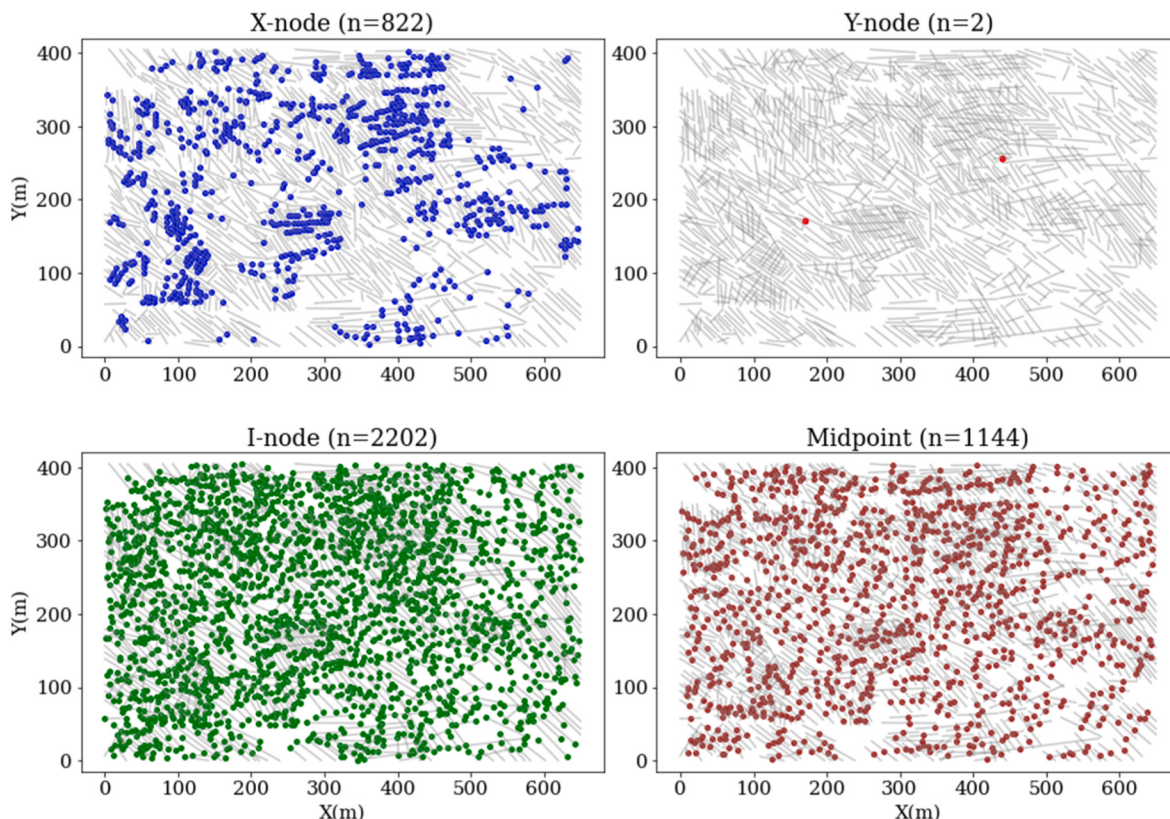


Fig. 14. Transformation of fracture network at Jabal Akhdar into point patterns for spatial analysis. Total number of nodes is given in parentheses above figures.

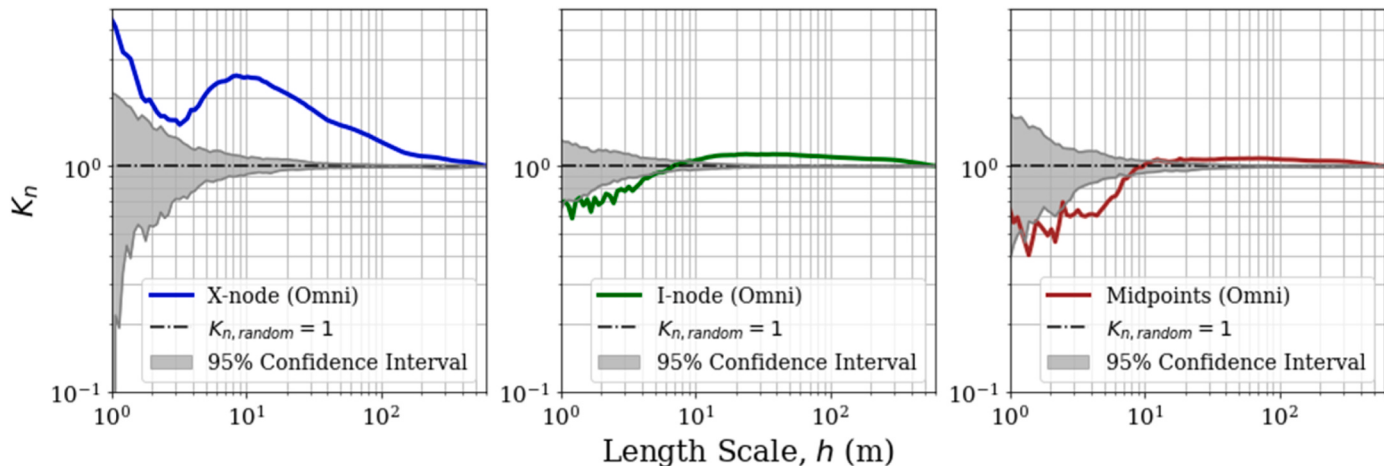


Fig. 15. Normalized omnidirectional K -functions calculated for fracture X-nodes (left), I-nodes (middle), and midpoints (right) at Jabal Akhdar, Oman.

fracture datasets from the literature.

3.1. Fracture network at Jabal Akhdar, Oman

The first fracture network case study is from the Mesozoic carbonates exposed on the southern flank of the Jabal Akhdar dome in Oman, published by Holland et al. (2009a, 2009b). Zeeb et al. (2013) manually digitized the fracture network from the images of the Quickbird satellite with a resolution of 0.7 m. The color contrast between bright cemented fractures and the gray host rock provides the opportunity to extract high-quality fracture network maps using remote sensing. The measured fracture dataset includes joints, veins, stylolites, and faults.

The fracture subset used in this work has 1144 lineaments (Zeeb

et al., 2013). Fig. 12 displays aerial views of the study area and the fracture traces. Fracture length ranges from 6 m to 220 m with a lognormal distribution. Fracture orientations range over many directions, most being between 120 and 150 strike angles. The strike angles are measured clockwise from north. Fig. 13 shows a histogram of fracture length and a rose diagram of fracture strike angle.

For spatial analysis using the K -function, the fracture network at Jabal Akhdar should be transformed into point patterns. The X-nodes, Y-nodes, I-nodes, and midpoints of fractures are extracted and superimposed on top of the fracture trace map (Fig. 14). There are 822 X-nodes, 2 Y-nodes, 2202 I-nodes, and 1144 midpoints. The fracture endpoints that fall on the boundaries of the study domain are not counted as I-nodes because those endpoints are artificially created as the

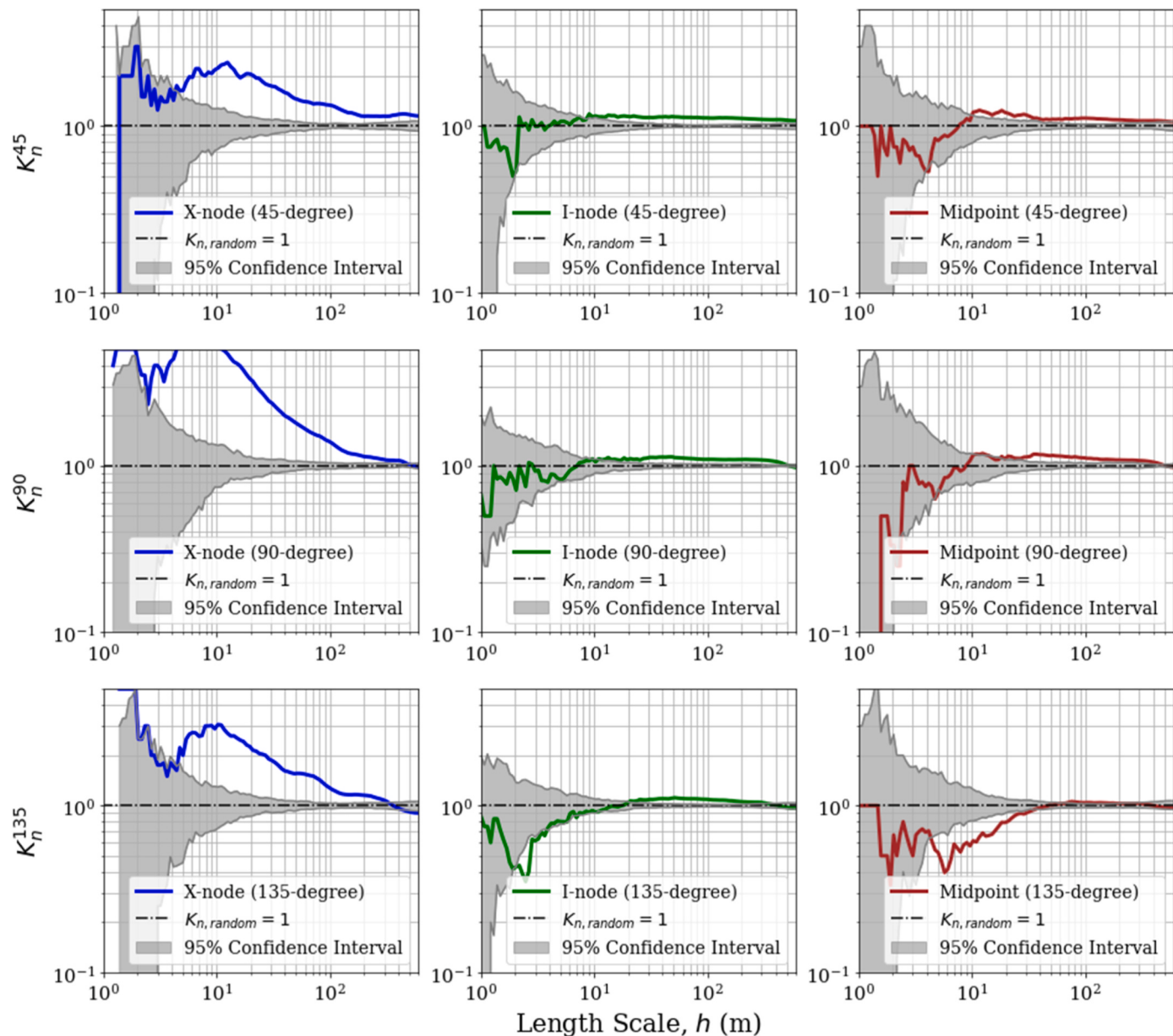


Fig. 16. Normalized directional K -functions calculated for fracture X-nodes (left column), I-nodes (middle column), and midpoints (right column) at Jabal Akhdar, Oman. Azimuths are 45° (top row), 90° (middle row), and 135° (bottom row).

result of truncating fracture traces that extend beyond the boundaries of the study domain.

The normalized omnidirectional K -functions calculated for the X-nodes, I-nodes, and midpoints are shown in Fig. 15. Because there are only two Y-nodes in this fracture dataset, the K -function is not calculated for the Y-nodes.

The normalized omnidirectional K -function for the X-nodes indicates that the spatial arrangement of fracture intersection points is clustered across all length scales. Visual inspection of the X-nodes in Fig. 14 also shows that the distribution of fracture intersection points is highly nonuniform, although fractures are propagated over the entire study domain. The X-nodes are sparse around the southern and northeastern corners of the domain. In these regions, most of the fractures are isolated. However, many X-nodes are clustered around the western and northern parts of the domain. Such regional clustering of fracture intersection points can impact fracture network connectivity and flow behavior in the subsurface.

Unlike the X-nodes, the I-nodes and midpoints exhibit antoclustered

arrangements at small length scales. For the I-nodes, the normalized omnidirectional K -function is less than the confidence interval at length scales of less than 5 m, representing an antoclustered arrangement. However, at length scales larger than 8 m, the normalized omnidirectional K -function exceeds the upper bound of the confidence interval, and the spatial arrangement becomes clustered. Similarly, for the midpoints, the spatial arrangement is antoclustered at length scales of less than 7 m, and clustered at length scales of greater than 15 m.

The antoclustering of fracture midpoints and I-nodes at small length scales implies that fractures are significantly farther apart from each other than if they had been distributed randomly. This inherent repulsion in fracture point patterns could be explained by geomechanical processes that govern fracture propagation, such as stress shadowing (e.g., Wu et al., 2012). Alternatively, the absence of fracture nodes near each other in the dataset could be because of limited imaging resolution and data sampling. Because fracture traces are digitized from satellite images, neighboring fractures with small lengths or aperture sizes might have been censored during data acquisition.

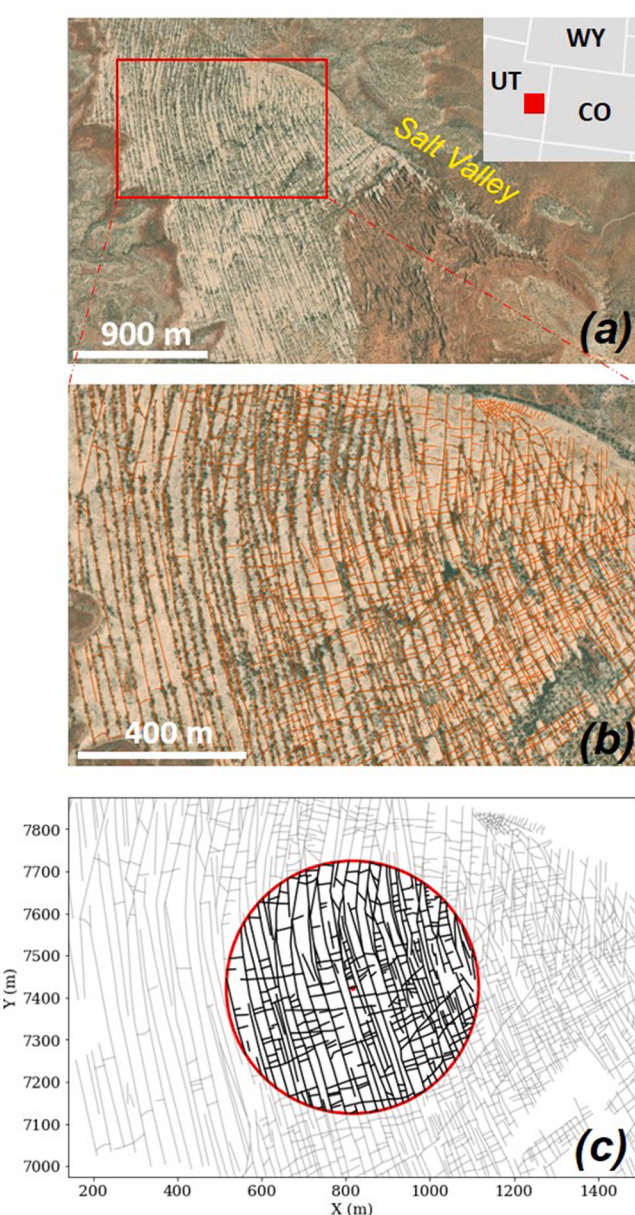


Fig. 17. Fracture network at Salt Valley, Utah, USA. (a) Satellite image of Salt Valley anticline and Moab sandstone exposed on the southwestern limb (from Geoplaner v3.1). (b) Digitized fracture network inside red rectangle (from Hanke et al., 2018). (c) A circular study domain with a radius of 300 m. The latitude and longitude of the center point are $38^{\circ}47'58.1''N$ and $109^{\circ}42'8.4''W$, respectively.

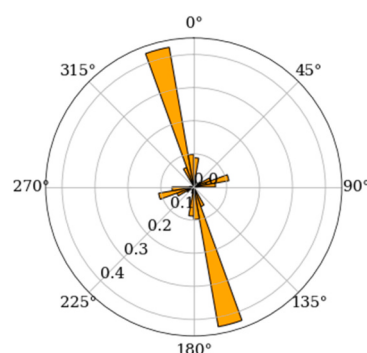
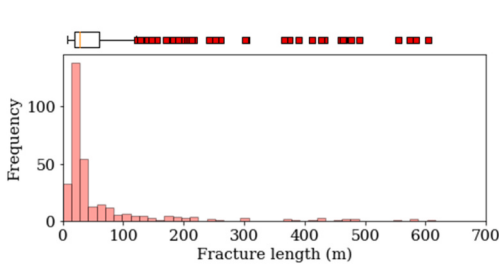


Fig. 18. Histogram and box plot of fracture length (left) and rose diagram of fracture strike angle weighted by fracture length (right) at Salt Valley, Utah.

At large length scales, the spatial arrangements of fracture midpoints and I-nodes become clustered. Although the spatial distribution of fracture midpoints and I-nodes may first appear random in Fig. 14, a close visual inspection reveals that fracture intensity is higher around the center and northwestern corner than in the eastern part of the domain. This regional clustering and proximity of fractures result in larger values of the K -function calculated for the fracture midpoints and I-nodes at large length scales.

In addition to the omnidirectional K -functions, the directional K -functions are calculated for the point patterns to investigate any directionalities in the dataset. The normalized directional K -functions are calculated for the 45-, 90-, and 135-degree azimuths (as illustrated in Fig. 16). The 90-degree and 135-degree azimuths are parallel to the dominant fracture sets (see rose diagram, Fig. 13), and the 45-degree azimuth is an arbitrary orientation. For each node type, the directional K -functions along different azimuths are approximately similar to those of the omnidirectional K -functions. This observation implies that the point patterns are isotropic, meaning that the spatial distributions of fracture nodes inside the study domain lack any major directionalities.

3.2. Fracture network at Salt Valley, Utah, USA

The second case study is from the Moab sandstone unit exposed on the southwestern limb of the Salt Valley anticline in Utah, USA (Fig. 17a). The fracture network is digitized from aerial images, processed, and assembled in a Geographic Information System (GIS) database by Hanke et al. (2018) (Fig. 17b). Since the minimum resolution is 5 m, parallel fractures closer than 5 m are combined into a single fracture. Fracture types are predominantly joint and deformation band. A subset of fractures bounded inside a circular study domain of radius 300 m is selected for spatial analysis (Fig. 17c).

There are 330 fractures inside the circular study domain, with a logarithmic length distribution ranging from 7 m to 604 m. Fractures are classified into two major sets. These two sets are approximately perpendicular and are formed as a result of a 90-degree rotation in the stress field (Hanke et al., 2018). The longer fractures are parallel to the anticline trend and are oriented between 155- and 175-degree strike angles, whereas the shorter fractures are perpendicular to the anticline trend. Fig. 18 shows the length distribution and a weighted rose diagram of fracture orientations inside the study domain. Although the number of shorter fractures is much higher than the longer fractures, a larger portion of fracture trace lengths belongs to the longer fractures. Thus, to better represent the overall orientation of fractures, the rose diagram (the radius of the wedges) is weighted by the relative magnitudes of fracture lengths.

Fig. 19 displays the various types of fracture nodes that are extracted from the fracture network inside the circular domain. Unlike the previous case study, most of the fracture intersection points here are Y-nodes (abutments). The shorter fractures abut and connect the perpendicular through-going fractures. For such fracture networks the expected

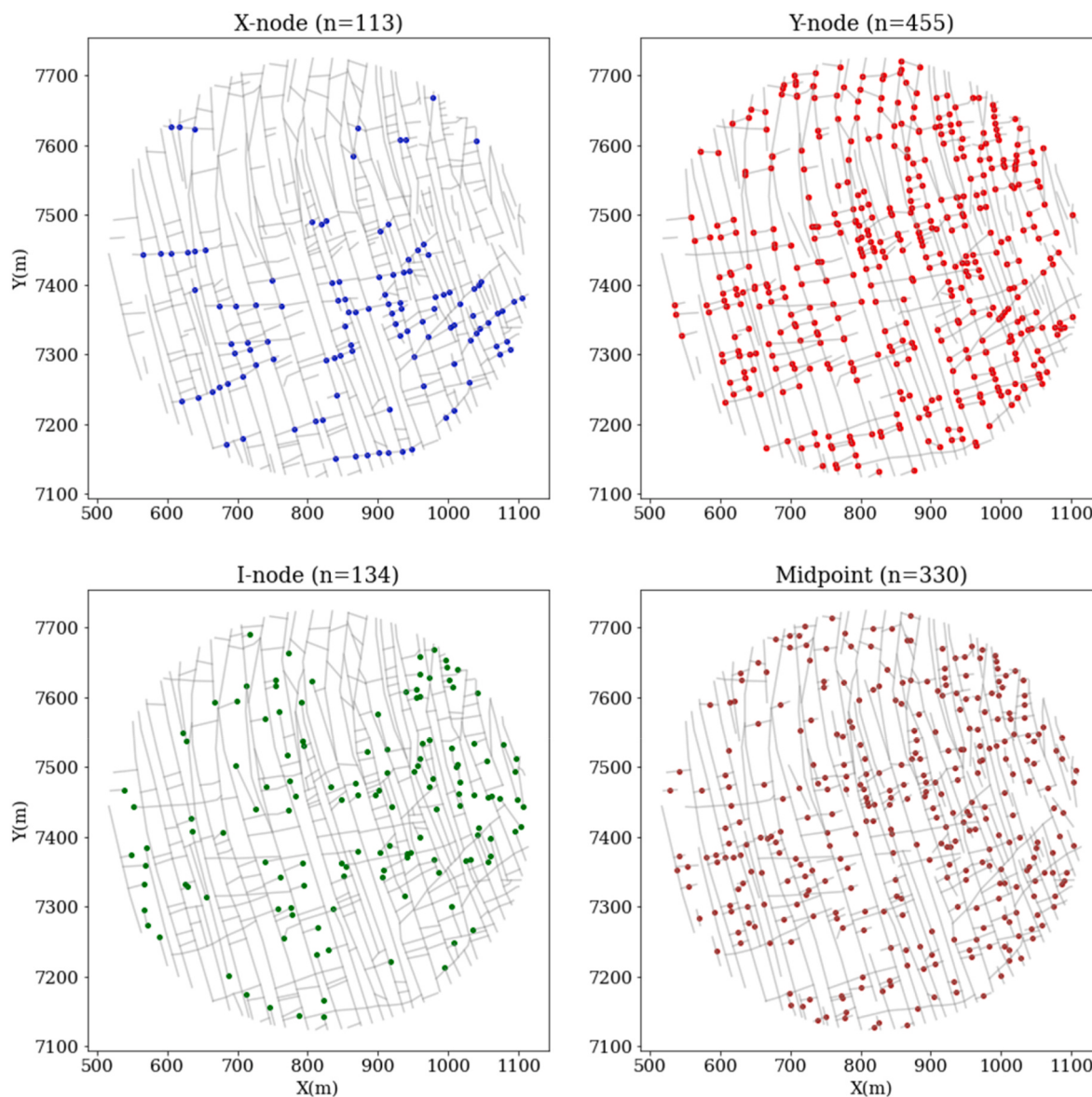


Fig. 19. Transformation of the fracture network at Salt Valley into point patterns for spatial analysis. Total number of nodes is given in parentheses.

degree of connectivity is relatively large because fracture intersection points (X-nodes plus Y-nodes) are scattered over the entire study domain. In addition, fracture abutments lower the number of isolated fracture tips (I-nodes). When a younger fracture grows into and abuts a preexisting fracture, an I-node is converted into a Y-node. If fracture propagation further continues, the Y-node is converted into an X-node, and a new I-node is also created. Therefore, the summation of the I-nodes and Y-nodes is constant in a fracture network. In this dataset, we have excluded the fracture tips that fall on the boundaries from the I-node population; they are synthetically generated because of the truncation of fracture traces that extend beyond the study domain.

The normalized omnidirectional K -functions calculated for the point patterns are shown in Fig. 20. Overall analysis of the K -functions indicates clustered spatial arrangements for the point patterns. For the X-nodes, the spatial arrangement is significantly clustered at length scales larger than 9 m. Visual inspection of Fig. 19 shows that most of the fracture X-nodes are clustered around the southern half of the study domain, where a few ENE-WSW-oriented fractures cross the perpendicular through-going fractures. For the Y-nodes, the spatial arrangement is clustered across all length scales. Although Y-nodes are scattered over the entire study domain, they form clusters of various sizes that

might not be evident by visual inspection. Additionally, the I-nodes exhibit a significantly clustered spatial arrangement at length scales larger than 30 m. At length scales smaller than 30 m, the normalized omnidirectional K -function for the I-nodes is still greater than 1, albeit inside the confidence interval for random arrangements. For the fracture midpoints, although the spatial arrangement is significantly clustered at length scales larger than 50 m, it becomes significantly antoclustered at length scales of less than 20 m. This is analogous to the observations made in the previous case studies of the spatial arrangement of fracture midpoints. At small length scales, the fracture midpoints are farther apart from what we expect to see from a random arrangement. This could be because of limited data resolution or geomechanical effects.

To investigate directionalities in the point patterns, the normalized directional K -functions are calculated for the 75-degree and 165-degree azimuths parallel to the directions of the two fracture sets. As all the nodes are located along the fracture traces, we expect that the two azimuths parallel to the fracture sets capture the anisotropic trends in the point patterns. Fig. 21 illustrates the results from the various node types. At length scales of less than 400 m, the normalized directional K -functions at both azimuths are approximately similar for each node. This indicates that the point patterns lack any significant directionalities at

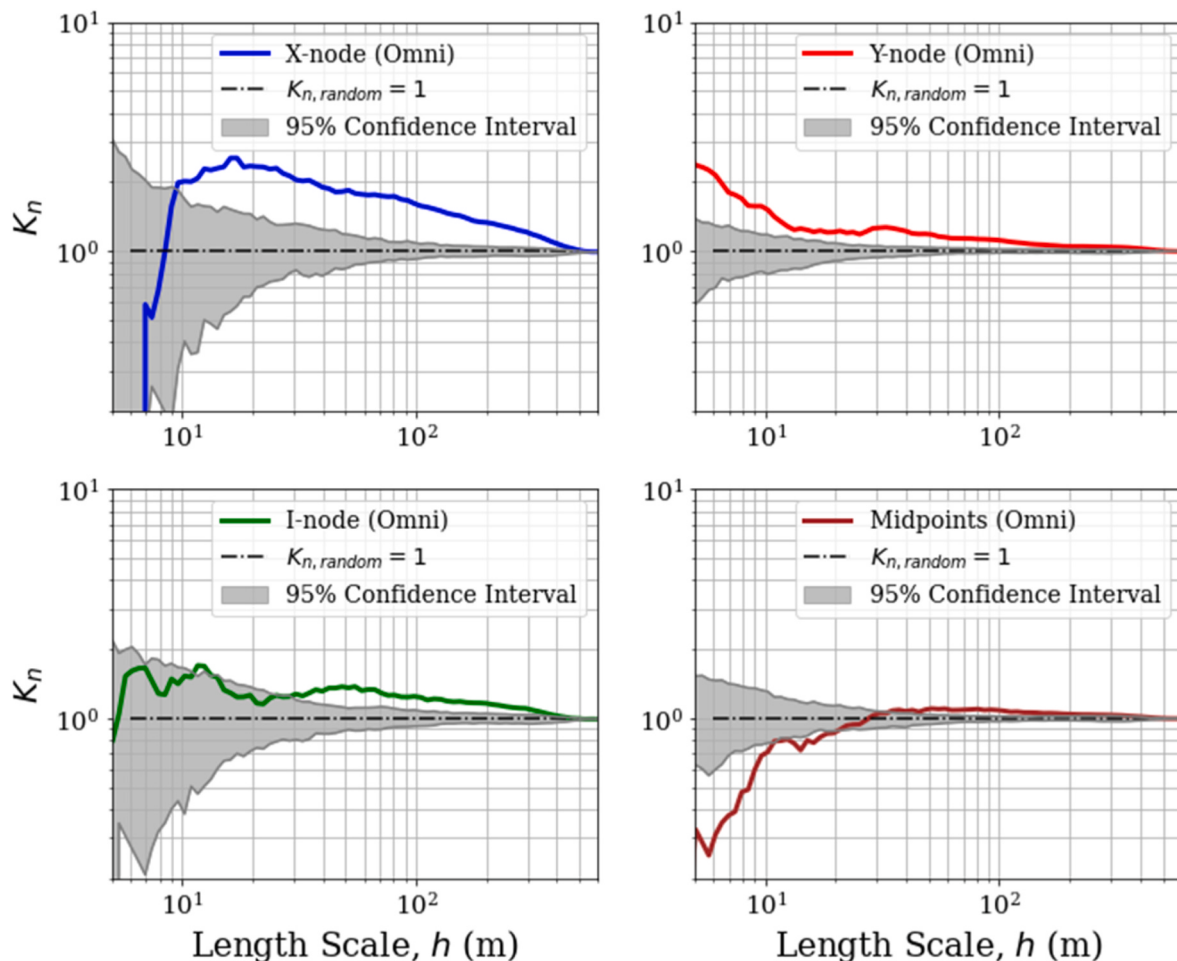


Fig. 20. Normalized omnidirectional K -functions calculated for fracture X-nodes, I-nodes, Y-nodes, and midpoints at Salt Valley, Utah.

those length scales. The minor differences, especially at small length scales, are mostly related to the lower number of points sampled in each direction compared to the omnidirectional calculations. Usually, for higher density point patterns such differences are diminished as more points are sampled at small length scales. At length scales larger than 400 m, however, some anisotropic behavior can be observed, particularly in the X-nodes and I-nodes. At these length scales, the normalized K -functions along the 75-degree azimuth are above the confidence interval for X-nodes and I-nodes indicating clustering arrangements, whereas along the 165-degree azimuth, the normalized K -functions are close to the lower boundary of the confidence interval that corresponds to anticlustered arrangements. Such anisotropic behavior can be also corroborated by a visual inspection of the fracture nodes in Fig. 19. In this figure, most of the X-nodes and I-nodes are located on the fractures with the 75-degree orientation. This configuration leads to a clustering arrangement of the nodes along the 75-degree azimuth and an anti-clustering arrangement in the perpendicular direction.

In the fracture case studies presented in this section, we used the K -function to identify various arrangements of fracture nodes. Note that the results of the spatial analysis here mainly apply to the study domains selected for these case studies, and they may not necessarily represent the whole fracture domain. This is a common observation because the spatial arrangement of fractures may significantly change from one region to another. Variations in subsurface rock properties, stress states, flow, and geochemical conditions may result in heterogeneous fracture patterns and non-stationary domains. Therefore, practitioners should perform spatial analysis of various study domains and also use other sources of information, such as field observations, for a more holistic

analysis of fracture patterns.

4. Conclusions

Spatial analysis of fracture arrangement has been conventionally limited to one-dimensional measurements using spacing data between semi-parallel fractures. This is because fracture traces in two dimensions may have variable trace lengths and orientations, making measurement of pairwise distances challenging. To extend the spatial analysis to two dimensions, we propose a spatial analysis technique using Ripley's K -function that applies to fracture nodes extracted from fracture traces — midpoints, intersection points, abutments, and tips. These nodes are proxies to fracture locations and interaction between fracture traces within a network. Using Ripley's K -function one can identify statistically significant clustering and anticlustering of fracture nodes across various length scales.

Spatial directionality and anisotropy commonly occur in fracture networks. To account for such effects in spatial arrangements, we have derived directional versions of the K -function formulation. Instead of full circular search windows, we use symmetric sectors along the azimuth of interest as search windows. Application of the directional K -function reveals whether geometric anisotropy or periodicity exists in point patterns. In addition, in regularly spaced clusters, the distance between clusters can be inferred from the distance between peaks or troughs in the K -function.

A limitation of this work is that replacing fractures with nodes eliminates many of the geometric attributes of fractures, such as length, height, strike angle, and aperture size. To incorporate these geometric

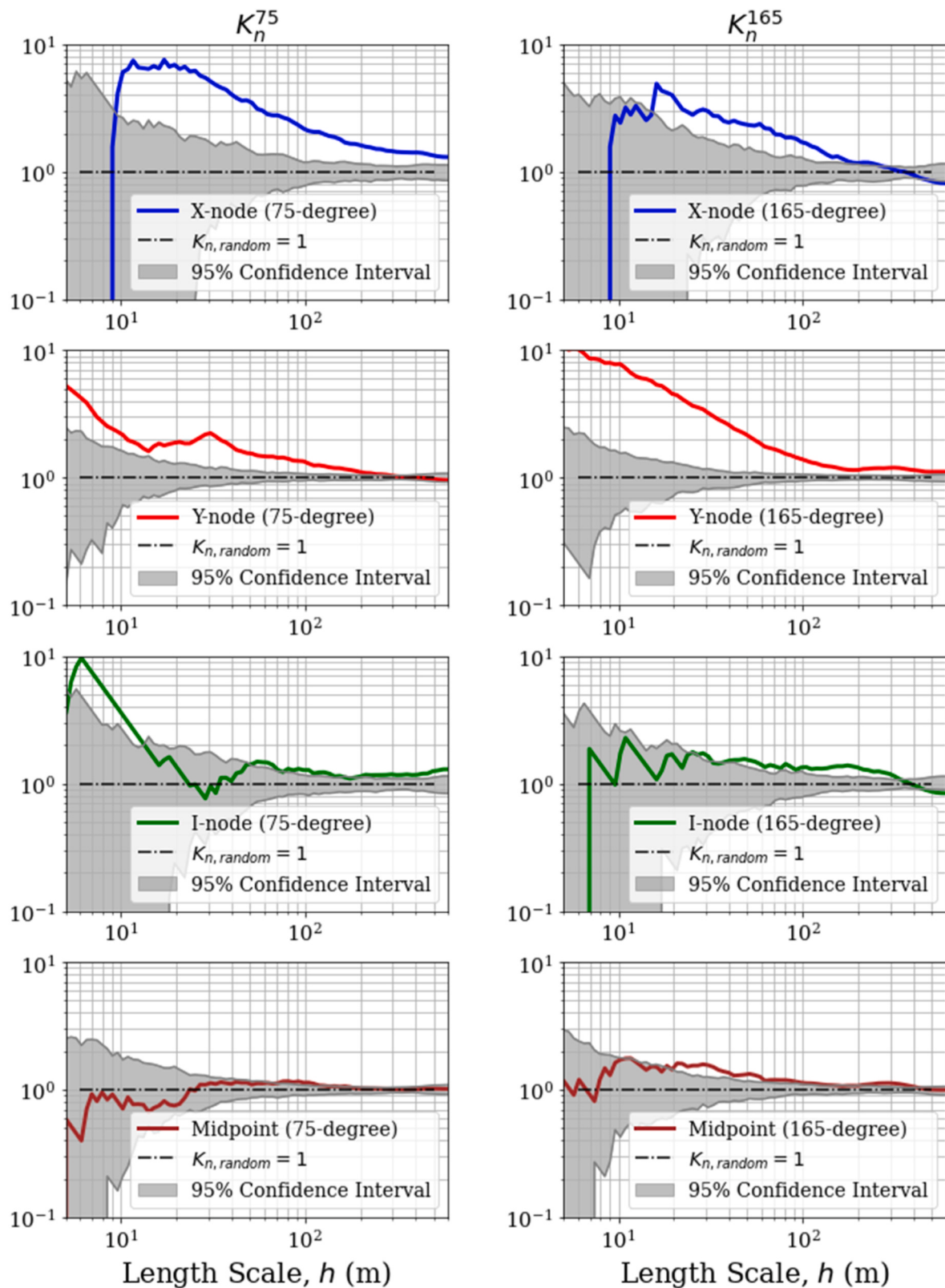


Fig. 21. Normalized directional K -functions calculated for fracture X-nodes (first row), Y-nodes (second row), I-nodes (third row), and midpoints (fourth row) at Salt Valley, Utah. Azimuths are 75° (left column) and 165° (right column), parallel to major orientations of fracture sets.

attributes into spatial analysis, one can assign their values to fracture midpoints. This modification allows application of other classes of methods, such as marked point pattern processes and semivariograms, for studying spatial variation of fracture attributes in the subsurface.

Also note that the spatial analysis in this work is performed on fracture nodes and not on fractures themselves. Any observed clustering or anticlustering exclusively refers to the arrangement of fracture nodes. Each node type exhibits a unique aspect of network geometry, and collectively they provide sufficient information to characterize and model fracture patterns. As an extension to this work, [Shakiba et al. \(2023b\)](#) introduce a novel approach using spatial arrangement of fracture nodes to statistically reconstruct synthetic fracture networks with spatial and flow behaviors similar to fracture networks observed on outcrops.

Declaration of competing interest

The authors declare that they have no known competing financial

interests or personal relationships that could have appeared to influence the work reported in this paper.

Data availability

Data will be made available on request.

Acknowledgments

This research was funded by grant DE-FG02-03ER15430 from Chemical Sciences, Geosciences and Biosciences Division, Office of Basic Energy Sciences, Office of Science, U.S. Department of Energy, and by The University of Texas Fracture Research and Application Consortium (FRAC). We thank Mark Fischer and John Hanke for processing and sharing the fracture dataset from Salt Valley, Utah. For the Jabal Akhdar case study, we used the fracture dataset published by [Zeeb et al. \(2013\)](#).

Appendix. Weighting Factors for Edge Correction in Two Dimensions

When calculating the K -function, part of the search window may fall outside the study domain for the data points that are near the edge or boundary. This results in an effectively smaller search area and consequently fewer number of neighbors counted around the boundary points. This is known as the edge effect. If edge effects are not corrected, the K -function will be underestimated. To correct for edge effects, weighting factors are used in the two-dimensional K -function formulations (Eqs. 5.1, 5.3, 5.6, and 5.8). To facilitate the calculation of the K -function in two dimensions, closed-form analytical expressions for the weighting factors are derived for circular and rectangular study domains.

A.1 Weighting Factors in Circular Study Domains

In a circular study domain, the weighting factors for edge correction can be derived for four different cases depending on the radius of the circular search window h (i.e., the length scale h), the radius of the study domain R , and the distance between the center of the study domain and the center of the search window, r . All possible cases are depicted in Fig. A1, where the red and blue circles are the study domain and the search window, respectively.

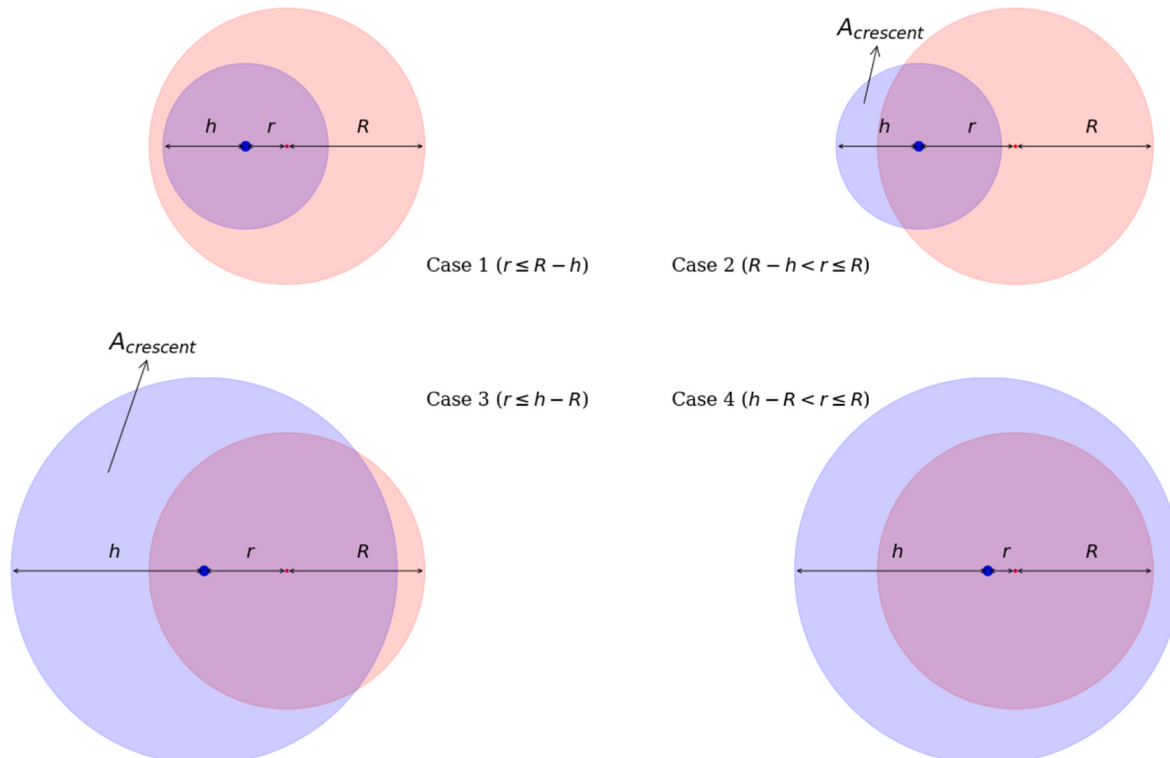


Fig. A1. Various geometric positions of a circular search window (in blue) inside a circular study domain (in red). Centers of search window and study domain are shown as blue and red dots, respectively. Four general cases are possible, depending on radius of circular search window h , radius of study domain R , and distance between centers of search window and study domain r . For each case, an analytical expression for edge correction is derived.

Case 1: $h \leq R$ and $r \leq R - h$

In this case, the search window is fully inside the study domain, therefore

$$\omega_i = 1 \quad (\text{A.1})$$

Case 2: $h \leq R$ and $R - h < r \leq R$

In case 2, the search window intersects the boundaries of the study domain. Also, the radius of the search window is smaller than the radius of the study domain.

$$\omega_i = \frac{\pi h^2}{\pi h^2 - A_{\text{crescent}}} \quad (\text{A.2})$$

Case 3: $R < h \leq 2R$ and $r \leq h - R$

Here, the search window is larger than the study domain, and it intersects the boundaries.

$$\omega_i = \frac{\pi h^2}{\pi h^2 - A_{\text{crescent}}} \quad (\text{A.3})$$

Case 4: $R < h \leq 2R$ and $h - R < r \leq R$

In this case, the search window is larger than the study domain, and it fully encompasses the study domain.

$$\omega_i = \frac{\pi h^2}{\pi R^2} \quad (\text{A.4})$$

In cases 2 and 3, A_{crescent} is the area of the blue crescent that falls outside the study domain (annotated in Fig. A1). This area is calculated using the following equations.

$$A_{\text{crescent}} = A_1 + A_2 - A_3 \quad (\text{A.5})$$

where

$$A_1 = 0.5 \sqrt{(h + R + r)(R + r - h)(h + R - r)(h + r - h)} \quad (\text{A.6})$$

$$A_2 = h^2 \cos^{-1} \left(\frac{R^2 - h^2 - r^2}{2hr} \right) \quad (\text{A.7})$$

$$A_3 = R^2 \cos^{-1} \left(\frac{R^2 - h^2 + r^2}{2Rr} \right) \quad (\text{A.8})$$

A.2 Weighting Factors in Rectangular Study Domains

The intersections between a circular search window and boundaries of a rectangular study domain can be divided into six general cases (Fig. A2). Parameters that determine the number and shape of intersections are the distances from the center of the search window to the sides of the rectangle (d_1 to d_4) and the radius of the search window h (i.e., the length scale h). Depending on the size of the search window, one or more cases of intersections may occur (combinations of cases 2 to 4).

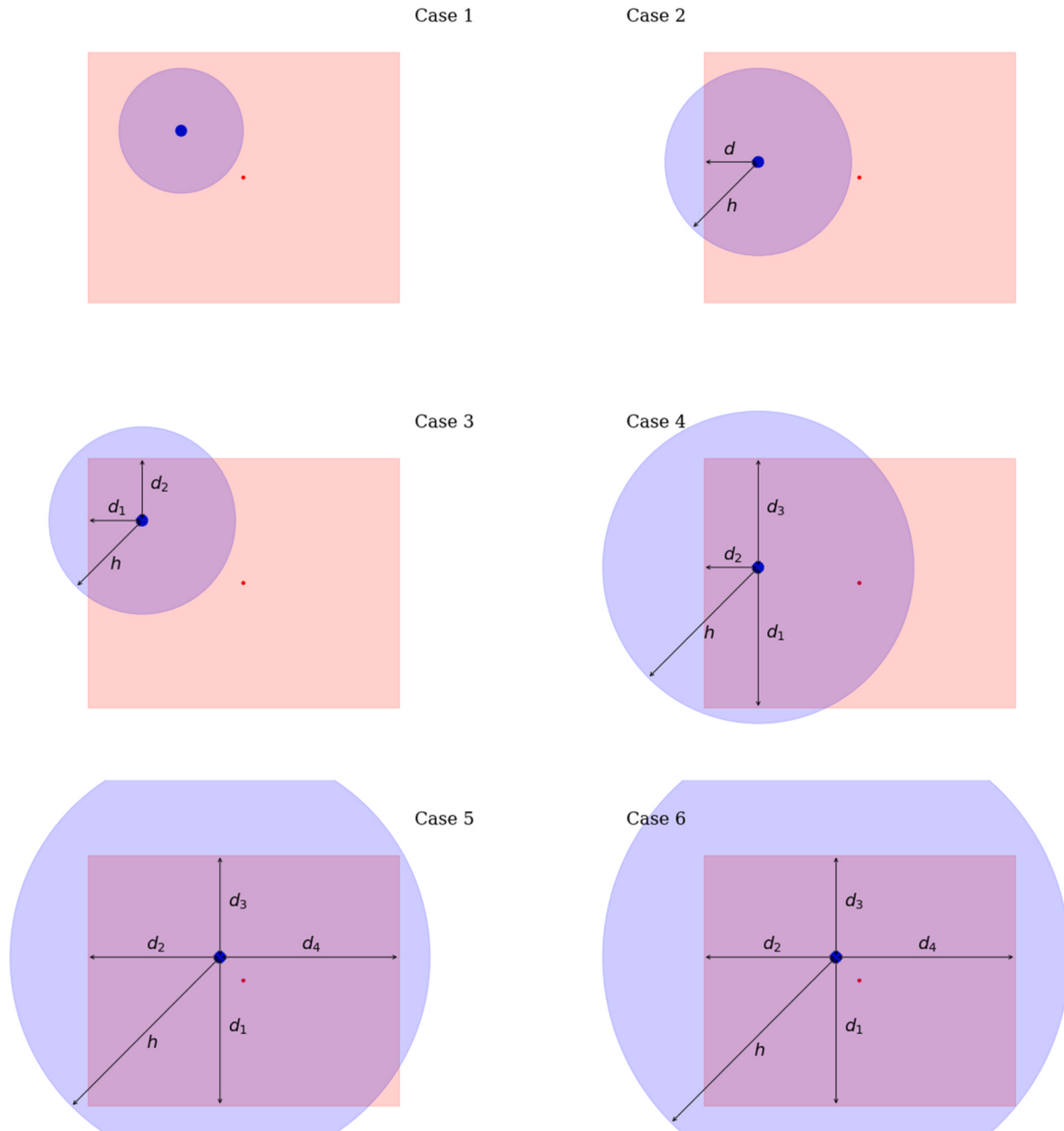


Fig. A2. Various geometric positions of a circular search window (in blue) inside a rectangular study domain (in red). Centers of search window and study domain are shown as blue and red dots, respectively. Six general cases are possible, depending on radius of circular search window h and distances between center of search window and sides of study domain, d_1 to d_4 . For each case, an analytical expression for edge correction is derived.

The general form of the weighting factors for edge correction is

$$\omega_i = \frac{\pi h^2}{\pi h^2 - A_{\text{outside}}} \quad (\text{A.9})$$

where A_{outside} is the summation of all the areas of the circular search window that lie outside the study domain. For each type of intersection in Fig. A2, A_{outside} is calculated using the following equations.

Case 1:

In this case, the circular search window is fully inside the study domain, therefore

$$A_{\text{outside}} = 0 \quad (\text{A.10})$$

Case 2: $d < h$

In case 2, the circular search window intersects a side of the rectangle, forming a secant, and all the corners are outside the circle.

$$A_{\text{outside}} = h^2 \cos^{-1} \left(\frac{d}{h} \right) - d\sqrt{h^2 - d^2} \quad (\text{A.11})$$

If the circular search window intersects more than one side of the rectangular study domain, Eq. A.11 should be calculated for each secant.

Case 3: d_1 and $d_2 < h$

In case 3, one corner of the rectangular study domain is inside the circular search window.

$$A_{\text{outside}} = \frac{\pi h^2}{4} + \frac{h^2}{2} \cos^{-1} \left(\frac{d_1}{h} \right) - \frac{d_1}{2} \sqrt{h^2 - d_1^2} + \frac{h^2}{2} \cos^{-1} \left(\frac{d_2}{h} \right) - \frac{d_2}{2} \sqrt{h^2 - d_2^2} - d_1 \times d_2 \quad (\text{A.12})$$

Case 4: d_1 , d_2 , and $d_3 < h$

In this case, two corners of the rectangular study domain are inside the circular search window.

$$A_{\text{outside}} = \frac{\pi h^2}{2} + \frac{h^2}{2} \cos^{-1} \left(\frac{d_1}{h} \right) - \frac{d_1}{2} \sqrt{h^2 - d_1^2} + \frac{h^2}{2} \cos^{-1} \left(\frac{d_3}{h} \right) - \frac{d_3}{2} \sqrt{h^2 - d_3^2} - d_2(d_1 + d_3) \quad (\text{A.13})$$

Case 5: d_1 , d_2 , d_3 , and $d_4 < h$

Here, three corners of the rectangular study domain are inside the circular search window.

$$A_{\text{outside}} = \frac{3\pi h^2}{4} + \frac{h^2}{2} \cos^{-1} \left(\frac{d_1}{h} \right) - \frac{d_1}{2} \sqrt{h^2 - d_1^2} + \frac{h^2}{2} \cos^{-1} \left(\frac{d_4}{h} \right) - \frac{d_4}{2} \sqrt{h^2 - d_4^2} - d_2(d_1 + d_3) - d_3(d_2 + d_4) + d_2 d_3 \quad (\text{A.14})$$

Case 6:

Finally, in case 6, the circular search window is larger than the study domain, and therefore it fully encompasses the study domain.

$$A_{\text{outside}} = \pi h^2 - (d_2 + d_4)(d_1 + d_3) \quad (\text{A.15})$$

References

- Baddeley, A., Bárány, I., Schneider, R., 2007. Spatial point processes and their applications. Stochastic Geometry: Lectures Given at the CIME Summer School Held in Martina Franca, Italy September 13–18, 1–75.
- Barton, C., Larsen, E., 1985. Fractal geometry of two-dimensional fracture networks at Yucca Mountain, Southwest Nevada. In: Fundamentals of Rock Joints: Proceedings of the International Symposium on Fundamentals of Rock Joints (Bjorkkliden, Sweden).
- Bemis, S.P., Micklithwaite, S., Turner, D., James, M.R., Akciz, S., Thiele, S.T., Bangash, H.A., 2014. Ground-based and UAV-Based photogrammetry: a multi-scale, high-resolution mapping tool for structural geology and paleoseismology. *J. Struct. Geol.* 69, 163–178.
- Bistacchi, A., Mittempergher, S., Martinelli, M., Storti, F., 2020. On a new robust workflow for the statistical and spatial analysis of fracture data collected with scanlines (or the importance of stationarity). *Solid Earth* 11 (6), 2535–2547.
- Bonnet, E., Bour, O., Odling, N.E., Davy, P., Main, I., Cowie, P., Berkowitz, B., 2001. Scaling of fracture systems in geological media. *Rev. Geophys.* 39 (3), 347–383.
- Corrêa, R.S.M., Marrett, R., Laubach, S.E., 2022. Analysis of spatial arrangement of fractures in two dimensions using point process statistics. *J. Struct. Geol.* 163, 104726.
- Cressie, N., 2015. Statistics for Spatial Data. John Wiley & Sons Inc.
- Dixon, P.M., 2014. Ripley's K Function. Wiley StatsRef: Statistics Reference Online.
- Forstner, S.R., Laubach, S.E., 2022. Scale-dependent fracture networks. *J. Struct. Geol.* 165, 104748.
- Gillespie, P.A., Howard, C.B., Walsh, J.J., Watterson, J., 1993. Measurement and characterisation of spatial distributions of fractures. *Tectonophysics* 226 (1–4), 113–141.
- Hanke, J.R., Fischer, M.P., Pollyea, R.M., 2018. Directional semivariogram analysis to identify and rank controls on the spatial variability of fracture networks. *J. Struct. Geol.* 108, 34–51.
- Hardebol, N.J., Maier, C., Nick, H., Geiger, S., Bertotti, G., Boro, H., 2015. Multiscale fracture network characterization and impact on flow: a case study on the Latemar carbonate platform. *J. Geophys. Res. Solid Earth* 120 (12), 8197–8222.
- Holland, M., Urai, J.L., Muchez, P., Willemse, E.J., 2009a. Evolution of fractures in a highly dynamic thermal, hydraulic, and mechanical system—(I) Field observations in a Mesozoic carbonates, Jabal Shams, Oman Mountains. *GeoArabia* 14 (1), 57–110.
- Holland, M., Saxena, N., Urai, J.L., 2009b. Evolution of fractures in a highly dynamic thermal, hydraulic, and mechanical system—(II) Remote sensing fracture analysis, Jabal Shams, Oman Mountains. *GeoArabia* 14 (3), 163–194.
- Laubach, S.E., Lamarche, J., Gauthier, B.D., Dunne, W.M., Sanderson, D.J., 2018. Spatial arrangement of faults and opening-mode fractures. *J. Struct. Geol.* 108, 2–15.
- Laubach, S.E., Lander, R.H., Criscenti, L.J., et al., 2019. The role of chemistry in fracture pattern development and opportunities to advance interpretations of geological materials. *Rev. Geophys.* 57 (3), 1065–1111.
- Manzocchi, T., 2002. The connectivity of two-dimensional networks of spatially correlated fractures. *Water Resour. Res.* 38 (9), 1–20.
- Marrett, R., Gale, J.F., Gómez, L.A., Laubach, S.E., 2018. Correlation analysis of fracture arrangement in space. *J. Struct. Geol.* 108, 16–33.
- Mauldon, M., Dunne, W.M., Rohrbaugh Jr., M.B., 2001. Circular scanlines and circular windows: new tools for characterizing the geometry of fracture traces. *J. Struct. Geol.* 23 (2–3), 247–258.
- Narr, W., Schechter, D.S., Thompson, L.B., 2006. Naturally Fractured Reservoir Characterization. Society of Petroleum Engineers, Richardson, TX.
- Odling, N.E., 1997. Scaling and connectivity of joint systems in sandstones from western Norway. *J. Struct. Geol.* 19 (10), 1257–1271.
- Olson, J.E., 2008. Multi-fracture propagation modeling: applications to hydraulic fracturing in shales and tight gas sands. In: The 42nd US Rock Mechanics Symposium (USRMS) (San Francisco, California).
- Pyrz, M.J., Deutsch, C.V., 2003. The whole story on the hole effect. Geostatistical Association of Australasia, Newsletter 18, 3–5.
- Ripley, B.D., 1976. The second-order analysis of stationary point processes. *J. Appl. Probab.* 13, 255–266.
- Ripley, B.D., 1977. Modelling spatial patterns. *J. Roy. Stat. Soc. B* 39, 172–192.
- Rizzo, R.E., Healy, D., Heap, M.J., Farrell, N.J., 2018. Detecting the onset of strain localization using two-dimensional wavelet analysis on sandstone deformed at different effective pressures. *J. Geophys. Res. Solid Earth* 123 (12), 460–478.
- Rohrbaugh Jr., M.B., Dunne, W.M., Mauldon, M., 2002. Estimating fracture trace intensity, density, and mean length using circular scan lines and windows. *AAPG (Am. Assoc. Pet. Geol.) Bull.* 86 (12), 2089–2104.
- Roy, A., Perfect, E., Dunne, W.M., McKay, L.D., 2014. A technique for revealing scale-dependent patterns in fracture spacing data. *J. Geophys. Res. Solid Earth* 119 (7), 5979–5986.

- Sævik, P.N., Nixon, C.W., 2017. Inclusion of topological measurements into analytic estimates of effective permeability in fractured media. *Water Resour. Res.* 53 (11), 9424–9443.
- Sanderson, D.J., Nixon, C.W., 2015. The use of topology in fracture network characterization. *J. Struct. Geol.* 72, 55–66.
- Sanderson, D.J., Nixon, C.W., 2018. Topology, connectivity and percolation in fracture networks. *J. Struct. Geol.* 115, 167–177.
- Sanderson, D.J., Peacock, D.C., 2019. Measurement of geometry and linkage in vein arrays. *J. Struct. Geol.* 118, 104–113.
- Shakiba, M., Lake, L.W., Gale, J.F.W., Pyrcz, M.J., 2022. Multiscale spatial analysis of fracture arrangement and pattern reconstruction using Ripley's *K*-Function. *J. Struct. Geol.* 155, 104531.
- Shakiba, M., Lake, L.W., Gale, J.F.W., Pyrcz, M.J., 2023a. Characterization of spatial relationships between fractures from different sets using *K*-function analysis. *AAPG Bulletin*, In Review.
- Shakiba, M., Lake, L.W., Gale, J.F.W., Laubach, S.E., Pyrcz, M.J., 2023b. Stochastic reconstruction of fracture network pattern using spatial point processes. In Review.
- Sornette, D., Davy, P., 1991. Fault growth model and the universal fault length distribution. *Geophys. Res. Lett.* 18 (6), 1079–1081.
- Vollgger, S.A., Cruden, A.R., 2016. Mapping folds and fractures in basement and cover rocks using UAV photogrammetry, Cape Liptrap and Cape Paterson, Victoria, Australia. *J. Struct. Geol.* 85, 168–187.
- Walsh, J.J., Watterson, J., 1993. Fractal analysis of fracture patterns using the standard box-counting technique: valid and invalid methodologies. *J. Struct. Geol.* 15 (12), 1509–1512.
- Wang, Q., Laubach, S.E., Gale, J.F.W., Ramos, M.J., 2019. Quantified fracture (joint) clustering in Archean basement, Wyoming: application of the normalized correlation count method. *Petrol. Geosci.* 25 (4), 415–428.
- Weng, X., Kresse, O., Cohen, C., Wu, R., Gu, H., 2011. Modeling of hydraulic-fracture-network propagation in a naturally fractured formation. *SPE Prod. Oper.* 26 (4), 368–380.
- Wu, R., Kresse, O., Weng, X., Cohen, C.E., Gu, H., 2012. Modeling of interaction of hydraulic fractures in complex fracture networks. In: *SPE Hydraulic Fracturing Technology Conference*. The Woodlands, Texas.
- Zeeb, C., Gomez-Rivas, E., Bons, P.D., Virgo, S., Blum, P., 2013. Fracture network evaluation program (FraNEP): a software for analyzing 2D fracture trace-line maps. *Comput. Geosci.* 60, 11–22.